International Journal of Heat and Mass Transfer 141 (2019) 1036–1048

Contents lists available at ScienceDirect

International Journal of Heat and Mass Transfer

journal homepage: www.elsevier.com/locate/ijhmt

Numerical simulation of the impact of laying powder on selective laser melting single-pass formation

Liu Cao

Advanced Institute of Engineering Science for Intelligent Manufacturing, Guangzhou University, Guangzhou 510006, Guangdong, China

ARTICLE INFO

Article history:
Received 13 May 2019
Received in revised form 10 July 2019
Accepted 10 July 2019

Keywords:
Laying powder process
Selective laser melting
Discrete element method
Molten pool dynamics
Numerical simulation
Additive manufacturing

ABSTRACT

Selective laser melting (SLM) is an additive manufacturing technology to directly form complex metal parts. It has been demonstrated in aerospace and other fields. In the SLM single-pass formation process, the SLM layer distribution was modeled here via the discrete element method model (particle contact force model and particle motion equation). A dynamic behavior model of molten pool based on the particle scale was also established. The governing equations considered the influence of thermodynamic factors such as Marangoni effect, gasification recoil, and gasification heat dissipation. The laser energy model used a Gaussian heat source based on interface tracking. To study the influence of laying powder on SLM single-pass formation, the corresponding simulations were performed from three aspects: particle size distribution, powder bed tightness, and lamination thickness. To obtain a good formation zone in the actual SLM process, metal powder with a smaller average particle size should be used on the basis of saving money, and the proportion of large-sized particles in the powder should be minimized. A higher powder bed tightness is needed on the basis of ensuring a good connection with the substrate or the previous printed layer. Finally, a larger lamination thickness should be used on the basis of ensuring that the powder bed is sufficiently melted in the formation zone. This paper is expected to provide some guidance for the actual SLM laying powder process.

© 2019 Elsevier Ltd. All rights reserved.

1. Introduction

Based on the idea of "layering-superposition", the additive manufacturing technology can directly and quickly manufacture digital models into three-dimensional solid parts. It has a series of advantages such as high flexibility, no mold, and no structural restrictions [1]. Of these, selective laser melting (SLM) is an additive manufacturing technology to directly form metal parts. It has high formation precision and short formation cycle. This solves the problem of low formation efficiency of complex parts in traditional processes. It has been applied in aerospace, automotive, medical, and other fields [2]. However, the current SLM technology has a considerable distance from industrial applications—especially research on the mechanism of SLM formation and the influence of process parameters for further study.

The complex thermophysical interaction processes that exist during SLM formation often occur in a very short period of time and on a mesoscale scale. Relevant experimental studies focus on co-observations of the formation [3], laying powder [4], process parameters [5], part defects [6], microstructure characteristics [7], and mechanical properties of the parts [8]. These studies can explain the basic details of SLM formation; however, it is difficult to obtain accurate procedural information and quantitative analysis of the influence mechanism of various factors in experimental research. For example, the current engineering experimental methods cannot obtain the three-dimensional shape of the molten pool in the SLM formation. The numerical simulation technology has been widely used in industrial production for its visibility and forward-looking value. It is an effective technical means for studying physical processes and control defects of mechanical manufacturing [9,10].

SLM has outstanding advantages, but the physical process is very complicated. In the past ten years, numerical simulation research on the dynamic behavior of the molten pool in SLM formation has gradually emerged. These theoretical studies can be roughly divided into two directions: those based on the workpiece scale [11] and those based on the particle scale [12].

(1). Molten pool dynamics based on the workpiece scale

The so-called workpiece scale refers to the powder layer (including metal particles and voids) as a special material. This scale indirectly describes the temperature field and flow field

E-mail address: caoliu@gzhu.edu.cn

https://doi.org/10.1016/j.ijheatmasstransfer.2019.07.053
0017-9310/© 2019 Elsevier Ltd. All rights reserved.

evolution during SLM formation by setting equivalent physical parameters and flow behavior models. The mesh size is often a few hundred microns or even a few millimeters. During the calculation process of such a simulation method, the equivalent physical property parameters need to be adjusted based on the state of the powder layer (particle state, liquid and solid state), metal particle material, and powder bed tightness. The equivalent flow behavior model can only treat the metal phase and the gas phase as a whole. They can then artificially adjust the kinetic parameters (such as dynamic viscosity) based on the continuous medium [13–17]. Fig. 1 shows the temperature field and flow field results under different SLM scanning speeds calculated by Mukherjee *et al.* [15] based on the workpiece-scale method. This kind of simulation method can greatly reduce the calculation amount by equivalent processing to obtain the temperature, the shape of the molten pool, and the thermal deformation in the whole SLM-formation, however, it is impossible to directly describe the complex flow behavior of molten metal between particles due to the continuous treatment of the entire powder layer. Thus, the simulation accuracy is low.

(2). Molten pool dynamics based on the particle scale

The so-called particle scale refers to modeling based on the actual particle morphology. It directly calculates the heating and melting effect of the laser on the metal particles and describes the complex flow behavior of liquid metal between particles. The mesh size is often a few microns. This type of simulation method mainly involves two parts: the laying powder process and the molten pool dynamics.

A. Laying powder process

The laying powder process includes particle size distribution and powder bed distribution. Methods for obtaining particle size distribution are divided into artificial [18] (uniform size, bipolar distribution, normal distribution) and experimental [19] determination. The role of the powder bed distribution is to obtain the particle locations. The calculation methods include regular distribution [20], raindrop model [21], and discrete element method [22,23] (DEM). The key idea of DEM is to study the individual particles as the research object considering the normal and tangential contact between the particles, as well as the force between the particles and the roller. This can update the particle motion and position and obtain a powder bed distribution that is realistic. Fig. 2a shows the result of a single layer of powder via DEM.

B. Molten pool dynamics

The physical factors to be considered in the calculation of the molten pool dynamic behavior during the SLM formation include surface tension between the liquid metal and the substrate and particles, coupling between the gas phase and the liquid metal, Marangoni effect, gasification recoil, buoyancy, internal viscosity of the melt, gravity, and mushy zone drag force. Khairallah *et al.* [24] used the multiphysics code ALE3D to directly calculate the pore defect distribution at different SLM scanning speeds, but the influence of the Marangoni effect on the flow process was not considered. Tang *et al.* [25] analyzed the influence of surface tension and gasification recoil on pore defects during SLM formation based on the open source computational fluid dynamics code OpenFOAM (Fig. 2b). This kind of simulation method can directly describe the SLM formation and directly predict the formation and evolution of formation defects such as pore, spheroidization, and surface roughness. However, the calculation accuracy is greatly affected by physical modeling, and the calculation amount is often large. In addition, there is currently no simulation work on the impact of the actual laying powder process for SLM formation.

In this paper, the SLM layer distribution was obtained based on the discrete element method model (particle contact force model and particle motion equation). A dynamic behavior model of molten pool based on the particle scale was also established. The governing equations considered the influence of thermodynamic factors such as Marangoni effect, gasification recoil, gasification heat dissipation, etc. The laser energy model used a Gaussian heat source based on interface tracking. To study the influence of laying powder on SLM single-pass formation, the corresponding simulations were carried out from three aspects: particle size distribution, powder bed tightness, and lamination thickness. This paper is expected to provide some guidance for the actual SLM laying

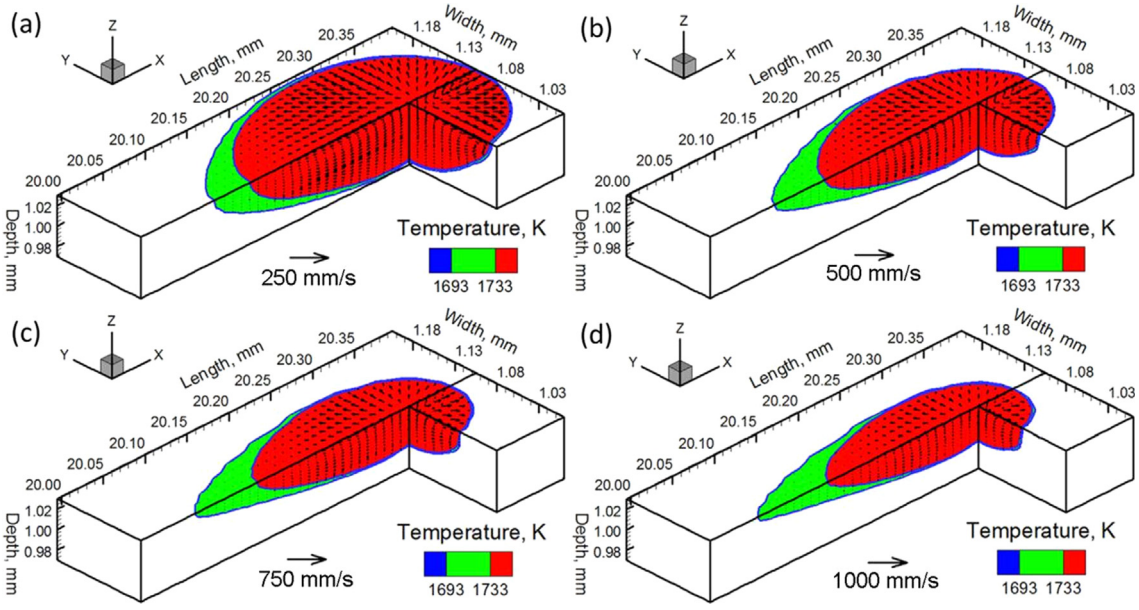

Fig. 1. Temperature field and flow field results under different SLM scanning speeds by using the method based on the workpiece scale [15].

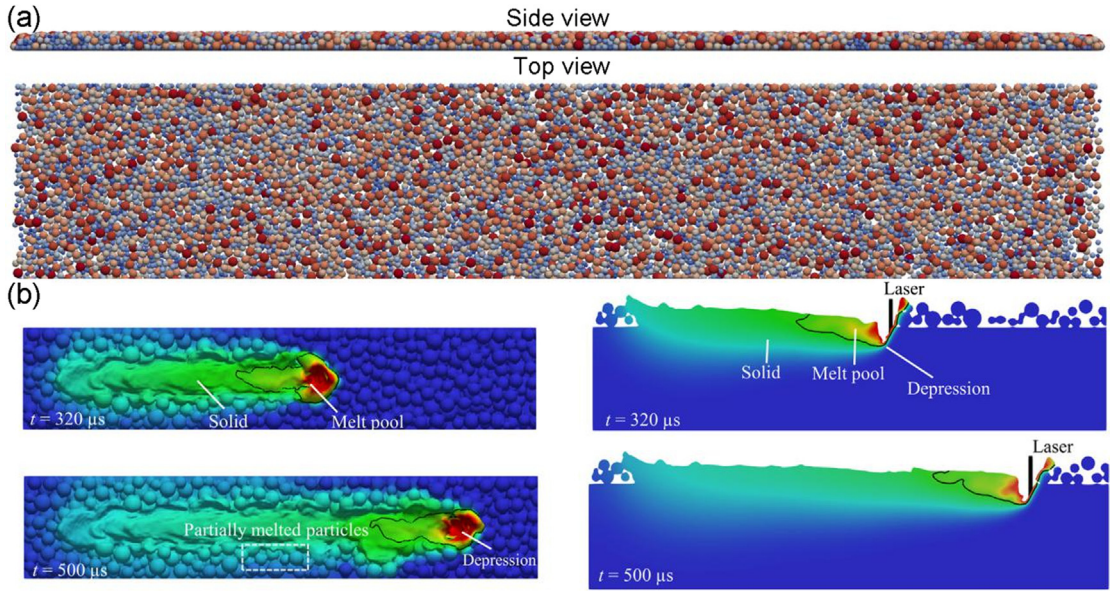

Fig. 2. Dynamic behavior simulation of molten pool based on the particle scale: (a) single layer result by using DEM; (b) SLM molten pool evolution results at different times [25].

powder process and provide a technical basis for the subsequent prediction of single-layer multi-pass and multi-layer multi-pass SLM formation in the large-scale computing domain.

2. Physical modeling and numerical solution

2.1. DEM model for laying powder

The actual powder bed distribution is a prerequisite for describing the SLM formation based on the particle scale. The SLM laying powder process is a typical multi-particle process considering that metal particles undergo slight deformation during the collision process. The shape of most metal particles may be considered as near-spherical; therefore, this paper uses a soft ball model to describe the relationship between force and displacement during particle collision. The soft ball model can be used to simulate the simultaneous collision of two or more particles, and the collision occurs within a certain period of time, and the contact force between the particles is then calculated according to the overlap between the spheres.

The soft ball model uses the vibrational motion equation to characterize the contact between particle and particle, as well as particle and boundaries. The normal and tangential decomposition of the vibrating motion of the particle contact process can be obtained, and the normal vibration equation during the particle contact process is:

$$m_e \frac{d^2 \boldsymbol{u}_n}{dt^2} + D_n \frac{d\boldsymbol{u}_n}{dt} + E_n \boldsymbol{u}_n = \boldsymbol{F}_n \tag{1}$$

The tangential vibrational motion of the particle contact process is characterized by tangential sliding and rolling:

$$m_e \frac{d^2 \boldsymbol{u}_t}{dt^2} + D_t \frac{d\boldsymbol{u}_t}{dt} + E_t \boldsymbol{u}_t = \boldsymbol{F}_t \tag{2}$$

$$\boldsymbol{I}_e \frac{d^2\theta}{dt^2} + \left(D_t \frac{d\boldsymbol{u}_t}{dt} + E_t \boldsymbol{u}_t \right) r = \boldsymbol{M} \tag{3}$$

where, m_e is the equivalent mass of particle i and particle j; $\boldsymbol{u}_n$ and $\boldsymbol{u}_t$ are the normal and tangential relative displacements of the particles, respectively; t is the time; D_n and D_t are the normal and tangential damping coefficients of the contact model, respectively; E_n and E_t are the normal and tangential elastic coefficients of the contact model, respectively; $\boldsymbol{F}_n$ and $\boldsymbol{F}_t$ are the normal and tangential components of the particle contact force, respectively; $\boldsymbol{I}_e$ is the equivalent moment of inertia; θ is the rotation angle of the particle itself; r is the radius of rotation; and $\boldsymbol{M}$ is the external torque of the particle.

The tangential sliding of the particles and the rolling of the particles are affected by the friction between the particles. The sliding model can establish the limit conditions for the tangential sliding and rolling of the particles:

$$\boldsymbol{F}_t = \mu E_n \boldsymbol{u}_n \mathrm{sgn}\left[E_t \left(\boldsymbol{u}_t + \frac{d\theta}{2} \right) \right] \tag{4}$$

Here, μ is the coefficient of friction, and sgn is the symbolic function.

After obtaining the contact force of the particles, the motion equation of the particle i is obtained as follows according to Newton's law of motion:

$$m_i \ddot{\boldsymbol{u}}_i = \boldsymbol{F}_{sum} \tag{5}$$

$$\boldsymbol{I}_i \ddot{\theta}_i = \boldsymbol{M}_{sum} \tag{6}$$

where, m_i is the mass of particle i; $\ddot{\boldsymbol{u}}_i$ is the acceleration of particle i; $\boldsymbol{F}_{sum}$ is the external force of particle i at the center of mass; $\boldsymbol{I}_i$ is the rotational inertia of particle i; $\ddot{\theta}_i$ is the angular acceleration of particle i; and $\boldsymbol{M}_{sum}$ is the external torque of particle i at the center of mass.

Using the Euler method to simultaneously integrate the two sides of Eqs. (5) and (6), the particle velocity $(\dot{\boldsymbol{u}}_i)_N$ and the angular velocity $\left(\dot{\theta}_i\right)_N$ of the next time step can be obtained:

$$(\dot{\boldsymbol{u}}_i)_N = (\dot{\boldsymbol{u}}_i)_{N-1} + \left(\frac{\boldsymbol{F}_{sum}}{m_i} \right)_N \Delta t \tag{7}$$

$$\left(\dot{\theta}_i\right)_N = \left(\dot{\theta}_i\right)_{N-1} + \left(\frac{\boldsymbol{M}_{sum}}{\boldsymbol{I}_i} \right)_N \Delta t \tag{8}$$

Simultaneous integration of both sides of Eqs. (7) and (8) gives the updated particle displacement $(\boldsymbol{u}_i)_{N+1}$ and the rotation angle $(\theta_i)_{N+1}$:

$$(\boldsymbol{u}_i)_{N+1} = (\boldsymbol{u}_i)_N + (\dot{\boldsymbol{u}}_i)_N \Delta t \tag{9}$$

$$(\theta_i)_{N+1} = (\theta_i)_N + \left(\dot{\theta}_i\right)_N \Delta t \tag{10}$$

Fig. 3 is the schematic diagram of SLM laying powder process. The process consists of four steps: (a) generating a cloud of particles above the substrate, (b) pushing the powder to the front of the roller, (c) the roller moving forward to lay powder, and (d) obtaining the powder bed with a certain thickness in the forming cavity.

2.2. Control equations of SLM molten pool dynamic behavior

In the study of SLM molten pool dynamic behavior based on the particle scale, solid phase metal particles are incapable of moving. When the particles are melted by laser radiation, the formed molten pool undergoes complex flow behavior, and the thermodynamic factors involved include heat absorption, heat conduction, heat convection, heat radiation, Marangoni effect, and gasification. Fig. 4 is the schematic diagram of SLM formation. In order to ensure the efficiency of numerical solution, four appropriate assumptions are made in this paper: The flow condition of the molten pool was considered to be an incompressible Newtonian fluid with laminar flow; The mass loss caused by metal gasification was not considered; The influence of metal density change on volume was not considered; and The spatter formation was not considered. In addition, since the solid particles were considered to be incapable of movement during the calculation, the denudation of the powder layer near of molten pool could not be considered. Next, the three types of conservation equations used in this paper will be introduced.

(1). Momentum conservation equation

To fully consider the various factors affecting the molten pool dynamic behavior during SLM formation, the calculation model used here is a two-phase flow model. The volume ratio factor of metal phase α_1 is used to indicate the volume fraction of metal phase at different positions: a value of 1 indicates that the position is completely occupied by the metal phase, and a value of 0 indicates that it is completely occupied by the gas phase. The value of the element at the interface is between 0 and 1. The equation governing the law of α_1 distribution is the volume ratio equation (VOF algorithm) [26]:

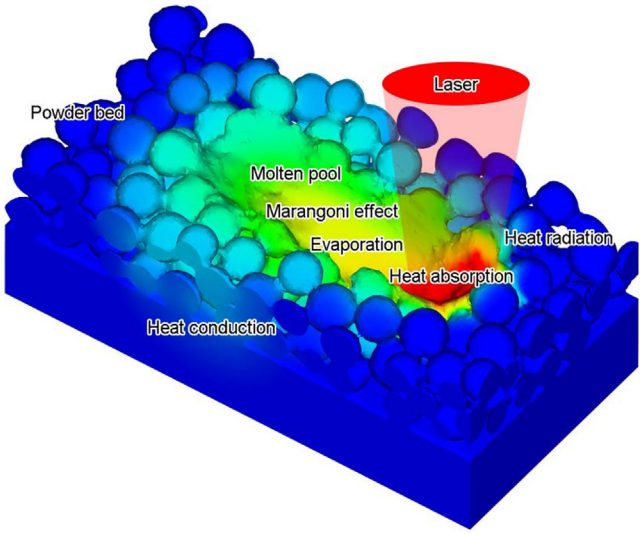

Fig. 4. Schematic diagram of SLM formation.

$$\frac{\partial \alpha_1}{\partial t} + \nabla \cdot (\alpha_1 \boldsymbol{u}) = 0 \tag{11}$$

$$\alpha_1 + \alpha_2 = 1 \tag{12}$$

where, α_1, α_2 are the element volume ratios of the metal phase and the gas phase, respectively; t is the time; and $\boldsymbol{u}$ is the velocity.

Through the distribution of α_1, the unit normal vector $\boldsymbol{n}$ at the interface can be obtained as:

$$\boldsymbol{n} = \frac{\nabla \alpha_1}{|\nabla \alpha_1|} \tag{13}$$

where, the direction of $\boldsymbol{n}$ is directed from the gas phase to the metal phase. Further, the curvature κ at the interface can be obtained as follows:

$$\kappa = -\nabla \cdot \boldsymbol{n} \tag{14}$$

The momentum conservation equation used is:

$$\frac{\partial \overline{\rho}\boldsymbol{u}}{\partial t} + \nabla \cdot (\overline{\rho}\boldsymbol{u} \otimes \boldsymbol{u}) = -\nabla p + \nabla \cdot \overline{\tau} + \overline{\rho}\boldsymbol{g} + \boldsymbol{F}_{mushy} + \left(\boldsymbol{F}_{tension} + \boldsymbol{F}_{Marangoni} + \boldsymbol{F}_{recoil}\right)|\nabla \alpha_1| \frac{2\overline{\rho}}{\rho_1 + \rho_2} \tag{15}$$

among them:

$$\overline{\rho} = \alpha_1 \rho_1 + \alpha_2 \rho_2 \tag{16}$$

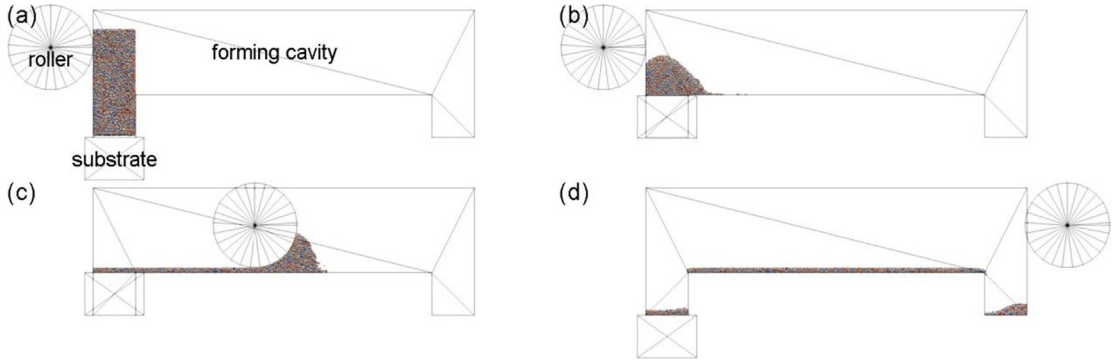

Fig. 3. Schematic diagram of SLM laying powder process: (a) start; (b) substrate push out powder; (c) roller lay powder; (d) finish.

$$\overline{\tau} = 2\overline{\mu}\left[\left(\frac{1}{2}\nabla \boldsymbol{u} + \frac{1}{2}(\nabla \boldsymbol{u})^T\right) - \frac{1}{3}(\nabla \cdot \boldsymbol{u})\mathbf{I}\right] \tag{17}$$

$$\boldsymbol{F}_{mushy} = -\overline{\rho}K_C\left[\frac{(1-f_l)^2}{f_l^3 + C_K}\right]\boldsymbol{u} \tag{18}$$

$$\boldsymbol{F}_{tension} = \sigma\kappa\boldsymbol{n} \tag{19}$$

$$\boldsymbol{F}_{Marangoni} = \frac{d\sigma}{dT}[\nabla T - \boldsymbol{n}(\boldsymbol{n}\cdot\nabla T)] \tag{20}$$

$$\boldsymbol{F}_{recoil} = 0.54P_0\exp\left[\frac{L_v m}{k_B}\left(\frac{1}{T_v} - \frac{1}{T}\right)\right]\boldsymbol{n} \tag{21}$$

where, $\overline{\rho}$, ρ_1, ρ_2 are respectively the mixed density, the metal phase density, and the gas phase density. Similarly, the same mixing treatment is performed for other physical parameters such as dynamic viscosity; $\otimes$ is the tensor product; p is the pressure; $\overline{\tau}$ is the stress tensor; $\overline{\mu}$ is the mixed dynamic viscosity; $\mathbf{I}$ is the unit matrix; $\boldsymbol{g}$ is the acceleration of gravity; $\boldsymbol{F}_{mushy}$ is the mushy zone drag force used to characterize the difference in fluidity caused by liquid-solid transition [27]; K_C is the permeability coefficient of porous media; C_K is a custom small value to avoid the drag force of the mushy zone during the calculation to infinity; f_l is the liquid fraction of metal phase; $\boldsymbol{F}_{tension}$ is the surface tension (the calculation model adopts the CSF (Continuum Surface Force) model) [28]; σ is the surface tension coefficient; and $\boldsymbol{F}_{Marangoni}$ is used to characterize the Marangoni effect. Here, the liquid surface temperature of the molten pool shows a central high and a low four-week state because the laser energy density is Gaussian in the horizontal plane. The liquid surface tangential flow occurs under the influence of the surface tension gradient because the surface tension is related to temperature [29]. In addition, $\frac{d\sigma}{dT}$ is the surface tension coefficient with temperature change rate; $\boldsymbol{F}_{recoil}$ is the gasification recoil of liquid metal; P_0 is the ambient pressure; L_v is the latent heat of vaporization; m is the molecular mass; k_B is the Boltzmann constant; T_v is the gasification temperature; and T is the temperature of liquid metal. In addition, the purpose of $|\nabla\alpha_1|$ in the rightmost term of Eq. (15) is to equivalent the surface force (surface tension, Marangoni effect, gasification recoil) to the volume force. The purpose of $\frac{2\overline{\rho}}{\rho_1+\rho_2}$ is to obtain a smooth force distribution near the surface of the molten pool.

(2). Energy conservation equation

The energy conservation equation used is:

$$\frac{\partial\overline{\rho c}_e T}{\partial t} + \nabla\cdot(\overline{\rho}\boldsymbol{u}\overline{c}_e T) = \nabla\cdot\left(\overline{k}\nabla T\right) - \left[(q_{con} + q_{rad} + q_{vap})|\nabla\alpha_1| - Q_{laser}\right]\frac{2\overline{\rho c}_e}{\rho_1 c_1 + \rho_2 c_2} \tag{22}$$

among them:

$$\overline{c}_e = \begin{cases} \alpha_1\left(c_1 + \frac{L_f}{T_l - T_s}\right) + \alpha_2 c_2 & T_l < T < T_s \\ \alpha_1 c_1 + \alpha_2 c_2 & T \geqslant T_l \text{ or } T \leqslant T_s \end{cases} \tag{23}$$

$$q_{con} = h_{con}(T - T_{con}) \tag{24}$$

$$q_{rad} = \sigma_s\varepsilon\left(T^4 - T_{rad}^4\right) \tag{25}$$

$$q_{vap} = 0.82\frac{L_v m}{\sqrt{2\pi m k_B T}}P_0\exp\left[\frac{L_v m}{k_B}\left(\frac{1}{T_v} - \frac{1}{T}\right)\right] \tag{26}$$

where, $\overline{c}_e$, c_1, c_2 are the equivalent specific heat capacity [30], the heat capacity of metal, and the heat capacity of gas, respectively; L_f is the latent heat of melting; T_l, T_s are the liquidus and solidus temperatures, respectively; $\overline{k}$ is the mixed thermal conductivity; q_{con} is the convection heat dissipation; h_{con} is the convective heat transfer coefficient; T_{con} is the ambient temperature at the gas-liquid interface; q_{rad} is the radiation heat dissipation; σ_s is the Stefan-Boltzmann constant; ε is the emissivity; T_{rad} is the radiation outside temperature; q_{vap} is the gasification heat dissipation of liquid metal; Q_{laser} is the laser energy density. In addition, the purpose of $|\nabla\alpha_1|$ in the rightmost term of Eq. (22) is to equivalent the surface heat dissipation (convection heat dissipation, radiation heat dissipation, and gasification heat dissipation) to the volume heat dissipation, and the purpose of $\frac{2\overline{\rho c}_e}{\rho_1 c_1 + \rho_2 c_2}$ is to obtain a smooth heat dissipation distribution near the surface of the molten pool.

The distribution of laser energy used in the SLM formation is Gaussian in the horizontal plane:

$$q_{laser} = \frac{2\eta P_{laser}}{\pi R^2}\exp\left(-2\frac{(x - x_0 - vt)^2 + (y - y_0)^2}{R^2}\right) \tag{27}$$

where, q_{laser} is the laser surface energy density; η is the laser absorption rate of the material; P_{laser} is the laser power; R is the laser spot radius; x_0, y_0 are the initial horizontal plane coordinates of the spot center; v is the rate at which the laser moves along the X-axis; and x, y are the horizontal coordinates of the spot center during laser movement.

Considering that the laser energy density is extremely high during the SLM formation, it is easy to cause the temperature field to be diverged when it is directly applied as a surface heat source. Therefore, this paper describes laser energy as a body heat source Q_{laser}:

$$Q_{laser} = \frac{f_{\Delta z} q_{laser}}{\Delta z} \tag{28}$$

where Δz is the equivalent size of the laser energy element such as the side length of the cube element, and $f_{\Delta z}$ is the energy ratio occupied by the element. During the calculation process, it is necessary to first track the initial layer interface element to which the laser spot is radiated in real time. Second, one should find the elements within a certain distance along the gravity direction with the first layer interface element as the starting point. Finally, the laser energy ratios are allocated based on the metal phase volume ratio of each element (the sum of the energy ratios of the single-column laser energy elements is one).

(3). Mass conservation equation

Since the fluids involved are considered to be incompressible fluids in the calculation process, the mass conservation equation is:

$$\nabla\cdot\boldsymbol{u} = 0 \tag{29}$$

2.3. Numerical solution

Combined with the above theoretical model, this paper first obtained the SLM powder bed distribution based on the open source DEM code Yade. Here, the geometric model of SLM laying powder process was introduced in the form of STL format. The metal particles are regarded as elastic materials with contact friction, and the roller was considered to be a rigid body. The SLM laying powder process—including the up and down movement of the substrate and the movement of the roller—was realized by a custom code. Second, the dynamic behavior of the SLM molten pool was calculated based on the finite difference method (FDM). The

flow field and thermal field were solved by the explicit algorithm with a calculation time step of 10 ns. Fig. 5 is the calculation flowchart.

3. Results and discussion

This paper used the above physical modeling and numerical solution process to simulate the influence of laying powder on the SLM single-pass formation. It then compared the results from three aspects: particle size distribution, powder bed tightness, and lamination thickness. In addition, the computing resources are configured as Intel Xeon Gold 5120 CPU (32 GB RAM).

3.1. Calculation parameters and mesh model

The material used in this paper is the 316L stainless steel, and its alloy composition (mass percentage) is Fe 65.395, C 0.03, Si 1.0, Mn 2.0, P 0.045, S 0.03, Ni 12.0, Cr 17.0, and Mo 2.5. Table 1 shows the required physical properties of 316L stainless steel [25]. Table 2 shows the heat source parameters used herein, and the absorption coefficient was considered to be a constant.

Fig. 6 is the adopted computing domain with an overall size of 1000 μm × 150 μm × 130 μm with a substrate thickness of 50 μm and a mesh size of 2.5 μm. During the calculation, the initial temperature was 300 K, the total formation was set to 600 μs, and the laser started to move from the horizontal coordinate (100 μm, 75 μm) with stops after 500 μs. In terms of computational efficiency, the average calculation time required for the SLM single-pass formation was 8 h.

To analyze the influence of particle size distribution, powder bed tightness, and lamination thickness on the SLM single-pass formation, the single-layer powder beds under different conditions were obtained by Yade (Table 3). The particle size distribution satisfies the normal distribution, and thus the average value and half width (the difference between the average value and the maximum or minimum value) are described. In addition, scheme A1 is the same as scheme B3 and scheme C2. A different naming convention is used to facilitate subsequent comparative analysis. The different powder bed tightness in schemes B1, B2, and B3 were obtained by setting different particle friction coefficients in Yade.

Table 1
Physical properties of 316L stainless steel [25].

Parameter	Value	Unit
Density of solid metal	7650	kg/m^3
Density of liquid metal	6870	kg/m^3
Specific heat of solid metal	596	J/(kg·K)
Specific heat of liquid metal	775	J/(kg·K)
Thermal conductivity of solid metal	$9.248 + 0.01571T$	W/(m·K)
Thermal conductivity of liquid metal	$12.41 + 0.003279T$	W/(m·K)
Solidus temperature	1658	K
Liquidus temperature	1723	K
Evaporation temperature	3090	K
Latent heat of melting	2.7×10^5	J/kg
Latent heat of vaporization	7.45×10^6	J/kg
Viscosity of liquid metal	0.00345	Pa·s
Surface tension	1.6	N/m
Temperature of surface tension	-8×10^{-4}	N/(m·K)
Molecular mass	9.3×10^{-26}	kg
Ambient pressure	101,325	Pa
Boltzmann constant	$1.3806505(24) \times 10^{-23}$	J/K
Emissivity	0.26	
Stefan-Boltzmann constant	5.67×10^{-8}	$W/(m^2 \cdot K^4)$

In the table, T is the temperature (K).

Table 2
Heat source parameters.

Parameter	Value	Unit
Laser spot diameter	54	μm
Scanning speed	1.5	m/s
Laser power	200	W
Absorption coefficient	0.35	

3.2. Influence of particle size distribution on SLM single-pass formation

The influence of particle size distribution on the SLM single-pass formation was analyzed first. Considering that the main parameters of particle size distribution are average value and half width, two kinds of comparison cases were set in this paper: The average value varies with a constant half width (A1, A2, A3, see Table 3), and a varying half width with a constant average value (A4, A5, A6, see Table 3). The powder bed distributions in the case where the average values are inconsistent and half widths are uniform are shown in Fig. 7. The number of particles in the single-layer powder bed is significantly reduced as the average particle size increases. The tightness of the large-sized particle powder bed is significantly lower.

Fig. 8 is the simulation results of the temperature field and the solid-phase fraction during the formation at different times in calculation scheme A1. The cross-sectional view is the Y-direction middle section of the calculation domain shown in Fig. 6. The metal particles were melted by heat to form the molten pool once the laser began to act on the powder bed; as the laser moved forward, new particles were continuously filled in the front of the molten pool, and the tail of the molten pool gradually cooled down to form

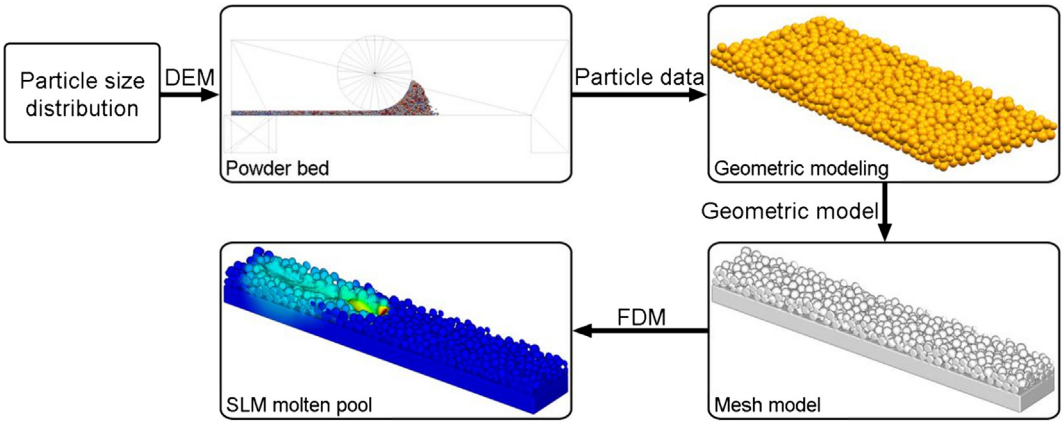

Fig. 5. Calculation flowchart.

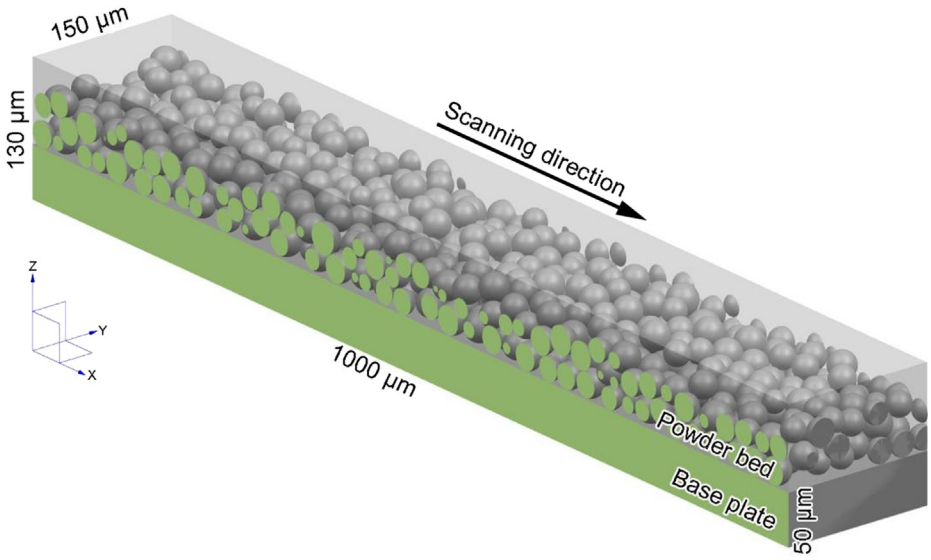

Fig. 6. Adopted computing domain.

Table 3
Single-layer powder beds with different particle size distribution, powder bed tightness, and lamination thickness.

Influencing factor	Calculation scheme	Particle size distribution		Powder bed tightness	Lamination thickness (μm)
		Average value (μm)	Half width (μm)		
Particle size distribution	A1	25	5	58.4737%	50
	A2	35	5	58.7699%	50
	A3	45	5	51.9563%	50
	A4	30	0	60.5049%	50
	A5	30	5	59.7262%	50
	A6	30	10	58.0671%	50
Powder bed tightness	B1	25	5	37.6437%	50
	B2	25	5	45.0412%	50
	B3	25	5	58.4737%	50
lamination thickness	C1	25	5	55.0183%	30
	C2	25	5	58.4737%	50
	C3	25	5	61.0047%	80

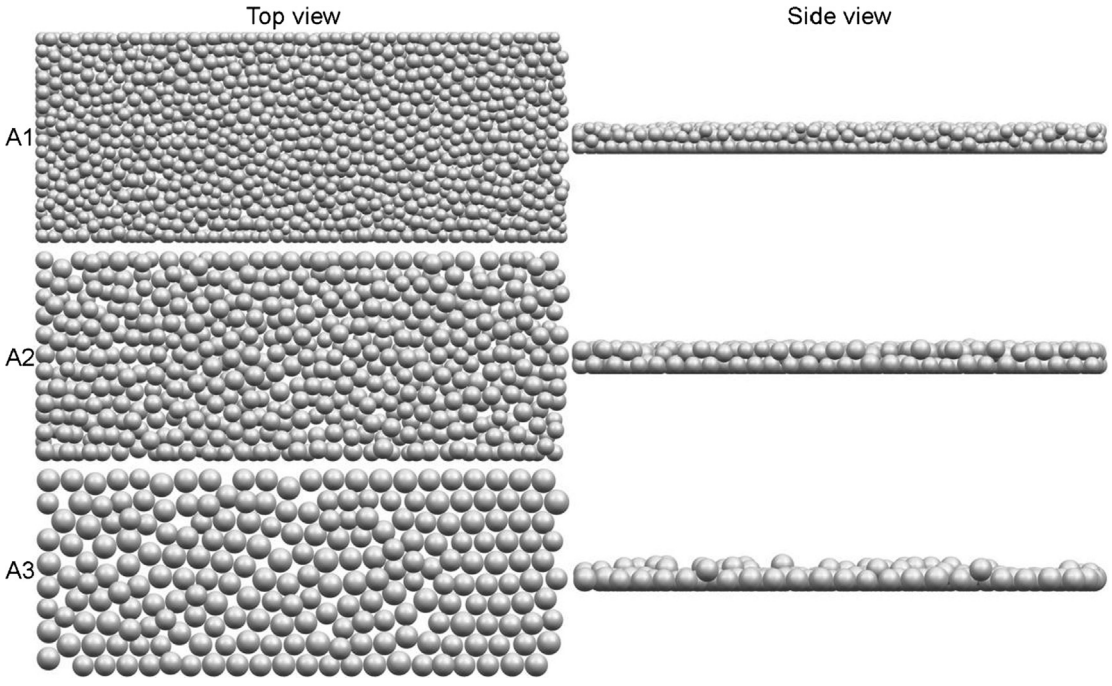

Fig. 7. Powder bed distributions of schemes A1, A2, and A3.

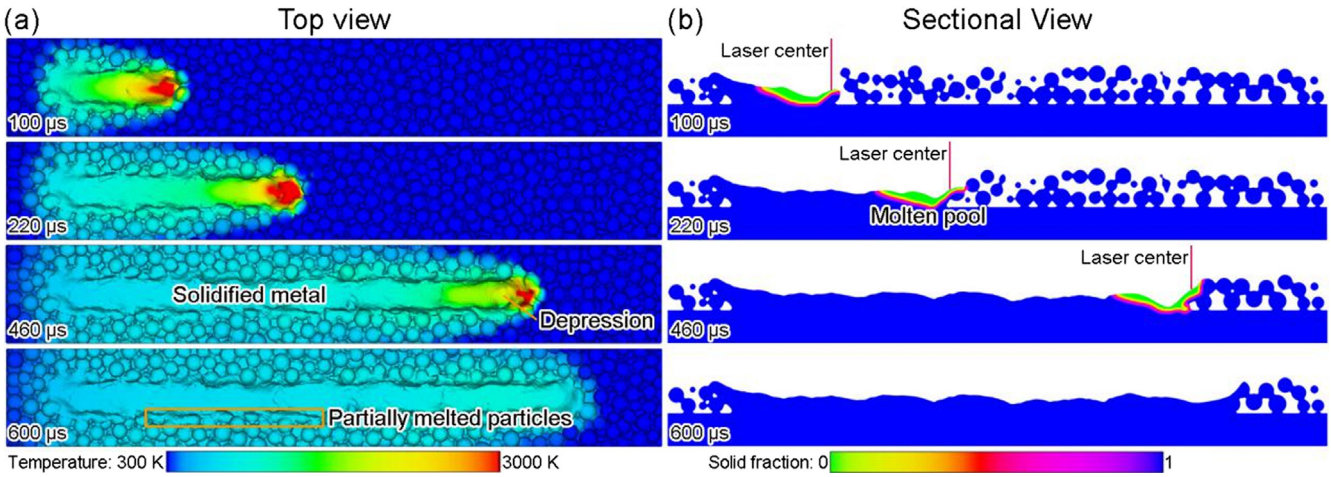

Fig. 8. Simulation results of temperature field and solid fraction in formation at different times in calculation scheme A1: (a) top view; (b) sectional view (Y = 75 μm).

the solidified track. Some of the substrate was also melted by heat and solidified. Finally, the area in which the laser acted in the powder bed formed the continuous solidified track. Fig. 9 shows the local temperature field and velocity field distributions of the middle section at a certain moment in the calculation scheme A1. The temperature of the molten pool surface area at the center of the spot was the highest since the energy density at the center of the laser spot was the largest. Gasification recoil force was generated in the liquid surface region when the temperature exceeded the metal vaporization temperature—this caused a significant downward movement. Due to the obvious liquid surface temperature gradient distribution in the rear part of the molten pool, Marangoni flow occurred in the liquid surface region, i.e., there was flow of the high-temperature liquid surface region to the low-temperature liquid surface region. Finally, the molten pool area showed obvious concave shape under the combined action of gasification recoil and Marangoni effect.

Fig. 10 is the simulation results of the final solidified track morphology of the calculation schemes A1, A2, and A3; Table 4 is the characteristic data of each solidified track. Here, the fluctuation value of the solidified track width refers to the variation range of the one-side boundary of the solidified track along the Y direction. The upper surface coordinate and the lower surface coordinate of the solidified track represent the contribution of the metal particles and the substrate to the solidified track, respectively. (This is the region solidified first after melting; the Z-axis coordinate of the upper surface of the substrate is 0 μm). The width of the solidified track and its fluctuation gradually increased as the average particle size gradually increased; the coordinate of the upper surface of the solidified track gradually decreased. The coordinate of the lower surface of the solidified track was significantly smaller when the average particle size was 45 μm. Powder bed with the small average particle size has a large amount of gas phase thermal resistance between the particles. When the average particle size was large, once the metal particles were locally heated, the heat was quickly conducted inside the particles. This made the width of the solidified track significantly larger, at the same time, the fluctuation of the solidified track width was also large due to the randomness of the particle distribution. The tightness of the powder bed was significantly lower with the average particle size of 45 μm (Table 3). The contribution of the metal particles to the solidified track was small, ans thus the coordinate of the upper surface was small.

The powder bed distributions in the case where the half widths are varying and average values are constant are shown in Fig. 11. Particles with a smaller size were distributed between the large

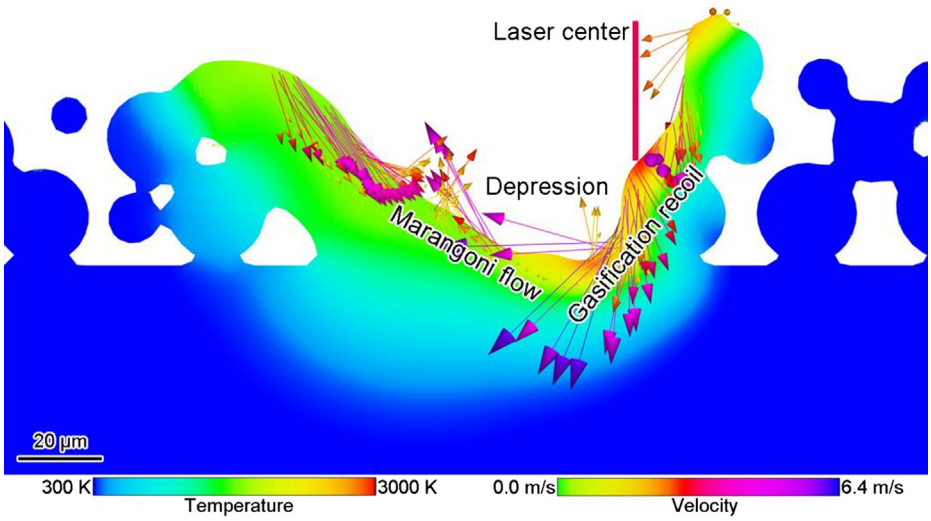

Fig. 9. Local temperature field and velocity field distributions of the middle section (Y = 75 μm) at 50 μs in calculation scheme A1.

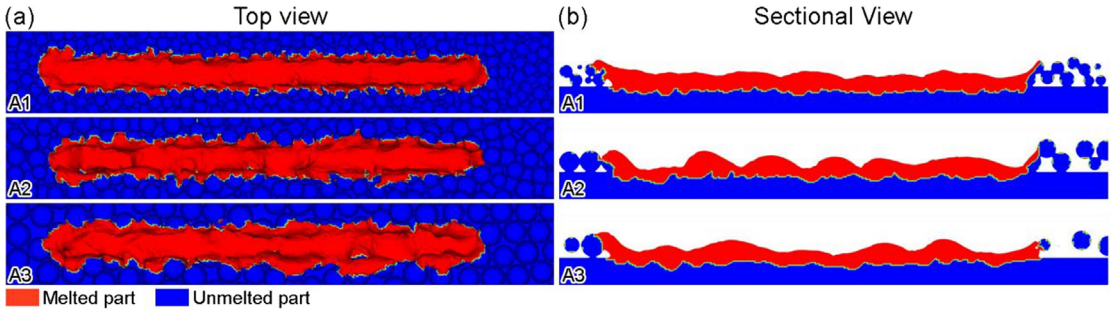

Fig. 10. Final solidified track morphology simulation results for calculation schemes A1, A2, and A3: (a) top view; (b) sectional view (Y = 75 μm).

Table 4
Characteristic data of solidified tracks of calculation scheme A1, A2, and A3.

Calculation scheme	Solidified track width (μm)		Upper surface coordinate of solidified track (μm)		Lower surface coordinate of solidified track (μm)	
	Average value	Fluctuating value	Average value	Fluctuating value	AVERAGE value	Fluctuating value
A1	59.92	11.90	23.71	12.25	−9.88	7.90
A2	67.64	17.90	19.76	28.05	−9.87	11.46
A3	80.00	28.00	16.05	26.08	−14.04	16.05

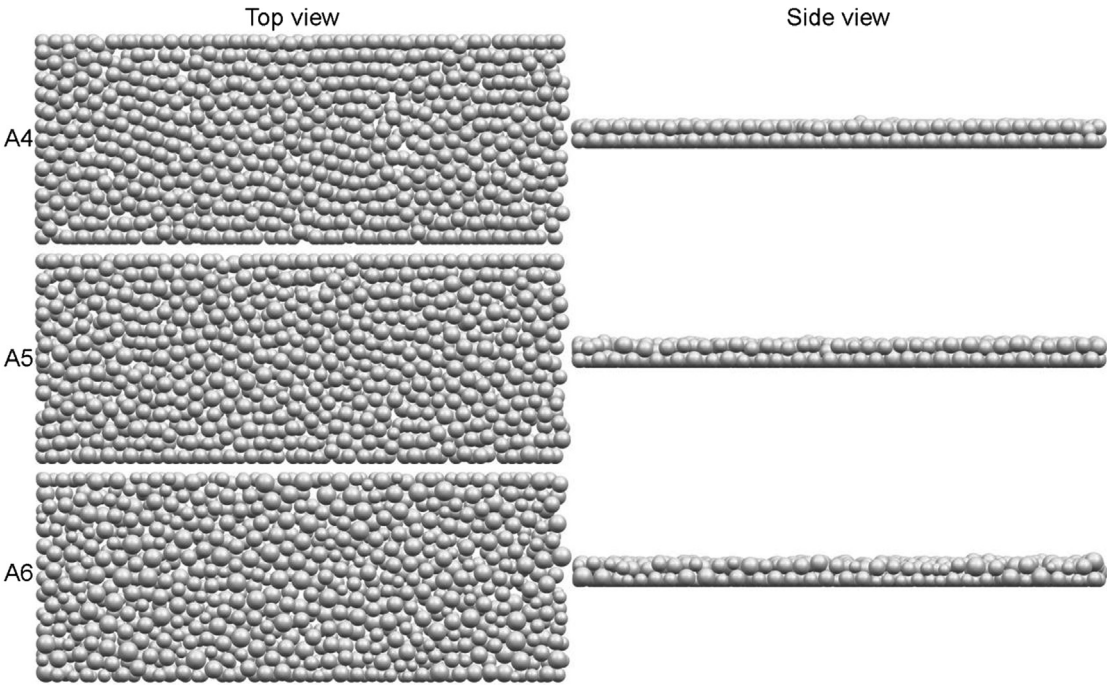

Fig. 11. Powder bed distributions of schemes A4, A5, and A6.

particles as the half width of the particle size increased gradually, i.e., a wider particle size distribution. This has a significant filling effect, which can improve the tightness of the powder bed.

Fig. 12 presents simulation results of the final solidified track morphology of the calculation schemes A4, A5, and A6. Table 5 is characteristic data of each solidified track. The results show that as the half width of the particle size increased gradually, the width of the solidified track remained basically constant, and its fluctuation was gradually increased; the coordinate of the upper surface was gradually decreased, and its fluctuation was gradually increased. The reason is that when the half width of particle size distribution was large, the large-sized particles in the powder bed gradually increased. Concurrently, the width fluctuation and the upper surface coordinate of the solidified track were large due to the randomness locations of the large-sized particle. Since the characteristic data fluctuation of the ideal SLM single-pass solidified track should be as small as possible to obtain a flat formation zone, the upper surface coordinate should be as large as possible to increase the height of the formation layer. The coordinate of the lower surface should be moderate to establish a good connection to the substrate or the previous printed layer. In summary, there is greater fluctuation in the solidified track characteristic data when there are more large particles in the particle size distribution, and there is larger the upper surface coordinate of the solidified track when there is higher tightness of the powder bed. Therefore, from the viewpoint of controlling the particle size

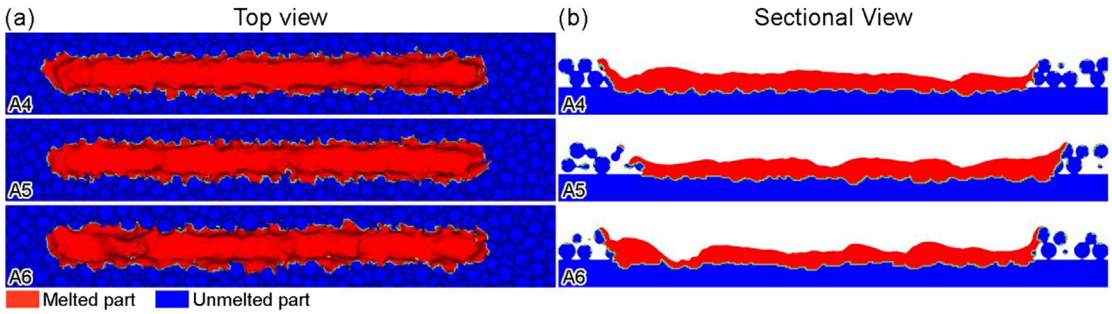

Fig. 12. Final solidified track morphology simulation results for calculation schemes A4, A5, and A6: (a) top view; (b) sectional view (Y = 75 μm).

Table 5
Characteristic data of solidified tracks of calculation scheme A4, A5, and A6.

Calculation scheme	Solidified track width (μm)		Upper surface coordinate of solidified track (μm)		Lower surface coordinate of solidified track (μm)	
	Average value	Fluctuating value	Average value	Fluctuating value	Average value	Fluctuating value
A4	67.74	14.11	24.19	16.13	−7.66	12.10
A5	67.11	19.74	23.81	19.84	−7.94	15.87
A6	70.84	23.75	15.87	33.73	−10.32	11.90

distribution, in order to obtain a good formation zone in the actual SLM production, metal powder with a small average particle size should be used on the basis of lower production costs, and the proportion of large-sized particles should be minimized.

3.3. Influence of powder bed tightness on SLM single-pass formation

The influence of the powder bed tightness on SLM single-pass formation was analyzed next, and the powder bed distribution under different powder bed tightness values is shown in Fig. 13. The powder bed tightness of calculation schemes B1, B2, and B3 were 37.6437%, 45.0412%, and 58.4737%, respectively (Table 3). Here, different powder bed tightness values were obtained by setting different particle friction coefficients in Yade. Fig. 13 shows that the particle arrangement under a low powder bed tightness was significantly looser.

Fig. 14 presents simulation results of the final solidified track morphology of calculation schemes B1, B2, and B3. Table 6 is characteristic data for each solidified track. The difference of the solidified track width and its fluctuation were small when the powder bed tightness increased gradually. Here, the coordinate of the upper surface gradually increased, and the coordinate of the lower surface also gradually increased. This is because the higher the powder bed tightness, the more the number of particles that were melted during the single-pass formation, so that the formation height of the solidified track was higher. In addition, the less energy was applied to the substrate or the previous printed layer, resulting in a reduction in the part of the substrate or the

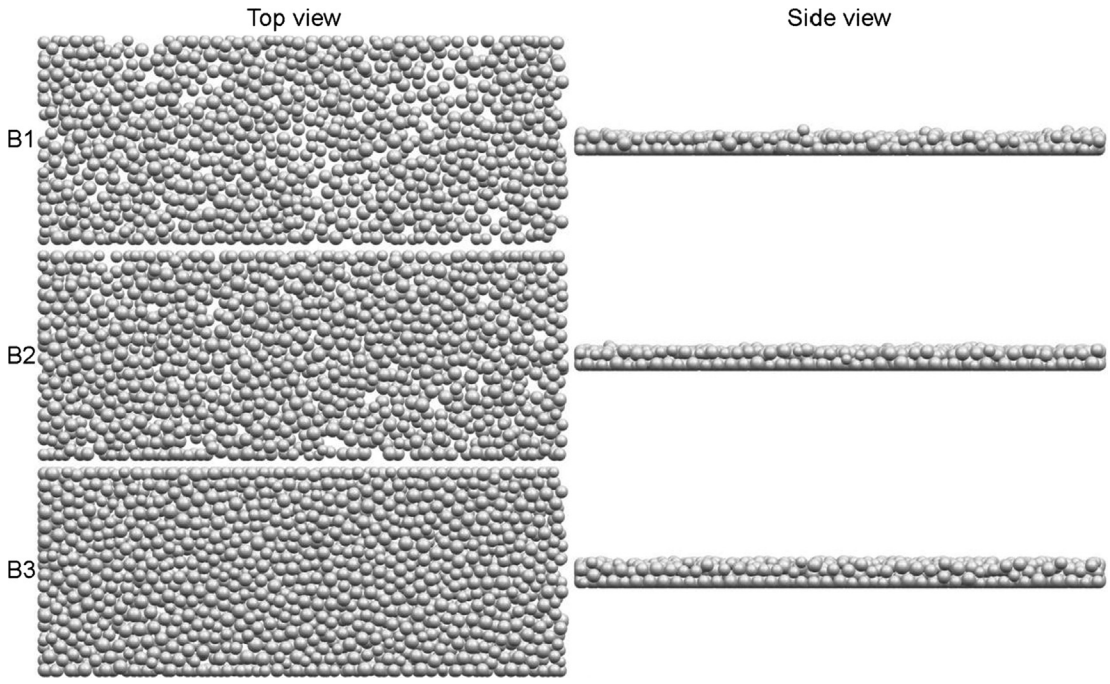

Fig. 13. Powder bed distributions of schemes B1, B2, and B3.

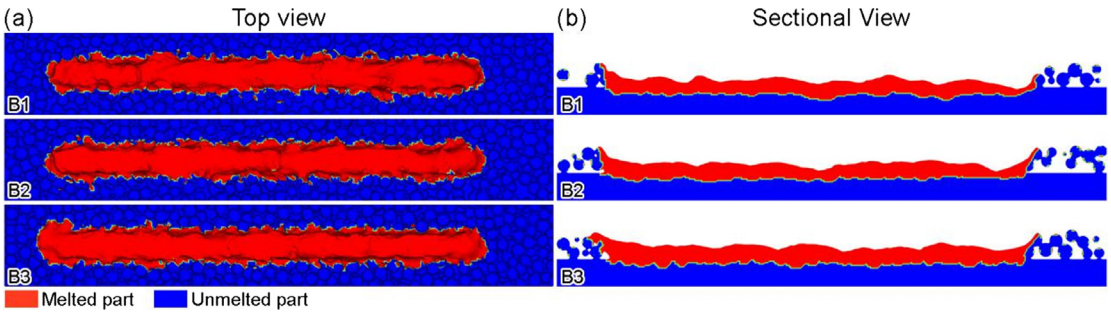

Fig. 14. Final solidified track morphology simulation results for calculation schemes B1, B2, and B3: (a) top view; (b) sectional view (Y = 75 μm).

Table 6
Characteristic data of solidified tracks of calculation scheme B1, B2 and B3.

Calculation scheme	Solidified track width (μm)		Upper surface coordinate of solidified track (μm)		Lower surface coordinate of solidified track (μm)	
	Average value	Fluctuating value	Average value	Fluctuating value	Average value	Fluctuating value
B1	64.29	13.89	15.63	15.62	−12.11	13.67
B2	63.55	13.82	18.60	19.38	−11.63	8.14
B3	59.92	11.90	23.71	12.25	−9.88	7.90

previously formed layer that was melted. Therefore, from the perspective of controlling the powder bed tightness, in order to obtain a good formation zone in the actual SLM production, it should be as high as possible on the basis of ensuring a good connection with the substrate or the previous printed layer, which is advantageous for obtaining a higher formation zone height and thus increasing production efficiency.

3.4. Influence of lamination thickness on SLM single-pass formation

Finally, the influence of the lamination thickness on SLM single-pass formation was analyzed, and the powder bed distributions under different lamination thickness values are shown in Fig. 15. The lamination thickness of the calculation schemes C1, C2, and C3 were 30 μm, 50 μm, and 80 μm, respectively (Table 3). Fig. 15 shows that the powder bed tightness increased as the lamination thickness increased.

Fig. 16 presents the simulation results of the final solidified track morphology of the calculation schemes C1, C2, and C3. Table 7 is characteristic data of each solidified track. The results show that as the lamination thickness increased, the coordinate of the upper surface of the solidified track increased significantly, and the coordinate of the lower surface also increased. When the lamination thickness was too large, a large amount of unmelted metal particles was present at the bottom of the powder bed resulting in a large number of pore defects in the lower portion of the solidified track. This is because when the lamination thickness was too large, the metal particles at the bottom of the powder bed could not

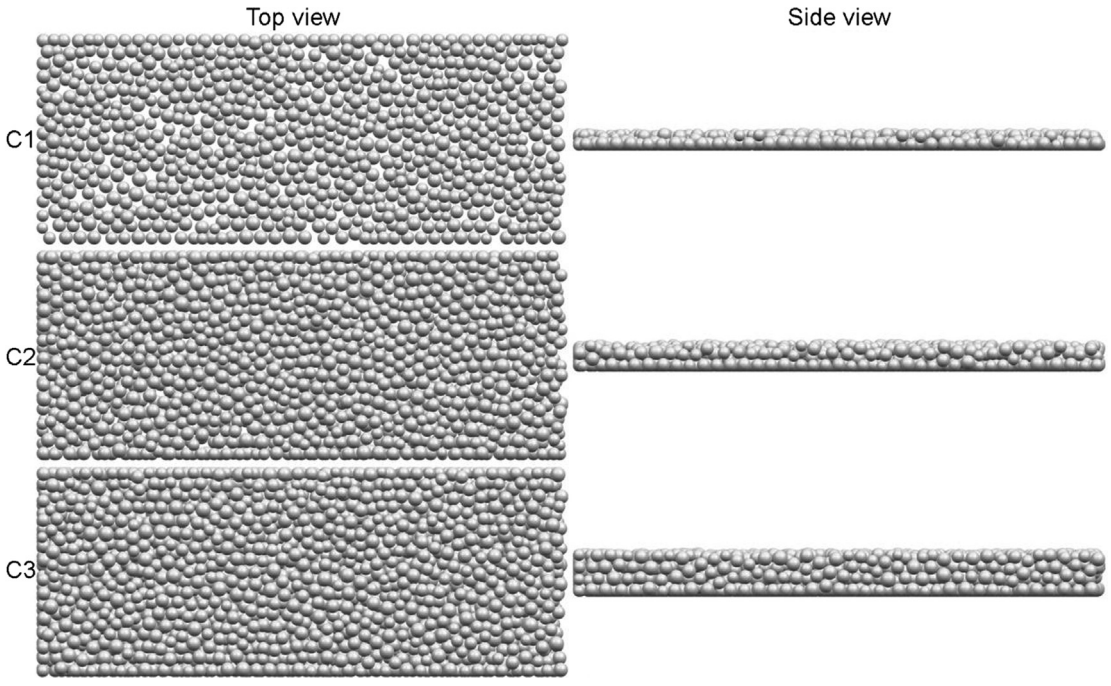

Fig. 15. Powder bed distributions of schemes C1, C2, and C3.

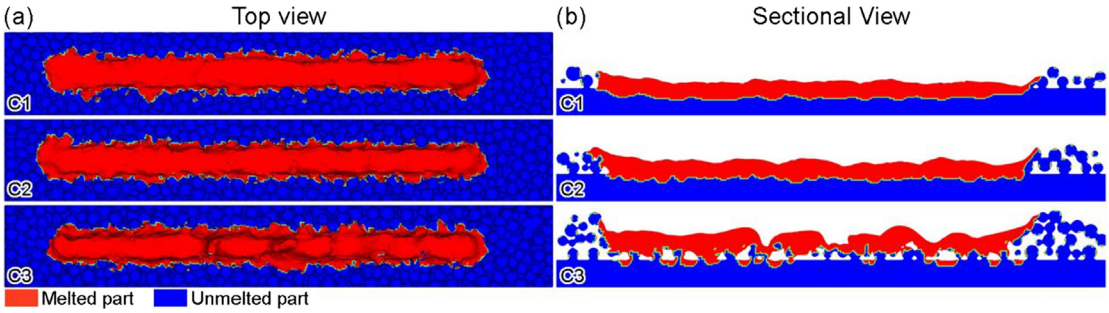

Fig. 16. Final solidified track morphology simulation results for calculation schemes C1, C2, and C3: (a) top view; (b) sectional view (Y = 75 μm).

Table 7
Characteristic data of solidified tracks of calculation scheme C1, C2, and C3.

Calculation scheme	Solidified track width (μm)		Upper surface coordinate of solidified track (μm)		Lower surface coordinate of solidified track (μm)	
	Average value	Fluctuating value	Average value	Fluctuating value	Average value	Fluctuating value
C1	65.13	19.74	14.84	13.67	−15.63	7.81
C2	59.92	11.90	23.71	12.25	−9.88	7.90
C3	67.28	16.62	Many particles were not melted on the lower part of the powder bed			

absorb sufficient laser energy. Therefore, from the viewpoint of controlling the lamination thickness, in order to obtain a good formation zone in the actual SLM production, on the basis of ensuring that the powder bed is fully melted in the formation zone, a larger lamination thickness should be used for improving production efficiency.

4. Conclusions

(1) The SLM powder bed distribution was obtained based on the open source DEM code Yade. The soft ball model was used to describe the relationship between force and displacement during particle collision, and the particle size distribution adopted a normal distribution.

(2) The dynamic behavior of SLM molten pool was predicted based on FDM. The governing equations considered the influence of thermodynamic factors such as Marangoni effect, gasification recoil, and gasification heat dissipation. The laser energy model used a Gaussian heat source based on interface tracking.

(3) In order to obtain the good formation zone in the actual SLM process, metal powder with a smaller average particle size should be used on the basis of ensuring the production cost, and the proportion of large-sized particles in the powder should be minimized. Concurrently, a higher powder bed tightness should be obtained on the basis of ensuring a good connection with the substrate or the previous printed layer. Finally, a larger lamination thickness should be used on the basis of ensuring that the powder bed is sufficiently melted in the formation zone.

(4) This paper evaluated the influence of laying powder on SLM single-pass formation. To further analyze the impact of laying powder on the performance of SLM parts, it is necessary to predict the single-layer multi-pass (interaction between neighbor tracks and scanning strategy sensitivity) and multi-layer multi-pass (influence of the previous printed layer) SLM formation in the large-scale computing domain. This is one of the key directions of subsequent research.

Acknowledgments

This work was supported by the Research Platform Construction Funding of Advanced Institute of Engineering Science for Intelligent Manufacturing, Guangzhou University.

Declaration of Competing Interest

I declare that I have no financial and personal relationships with other people or organizations that can inappropriately influence the work submitted.

References

[1] T. DebRoy, H.L. Wei, J.S. Zuback, et al., Additive manufacturing of metallic components–Process, structure and properties, Prog. Mater Sci. 92 (2018) 112–224.
[2] D. Wang, Z.Y. Qian, W.H. Dou, et al., Research Progress on selective laser melting of nickel based superalloy, Aeronaut. Manuf. Technol. 61 (10) (2018) 49–60.
[3] C.L.A. Leung, S. Marussi, R.C. Atwood, et al., In situ X-ray imaging of defect and molten pool dynamics in laser additive manufacturing, Nat. Commun. 9 (1) (2018) 1355.
[4] M.J. Xia, D.D. Gu, G.Q. Yu, et al., Porosity evolution and its thermodynamic mechanism of randomly packed powder-bed during selective laser melting of Inconel 718 alloy, Int. J. Mach. Tools Manuf 116 (2017) 96–106.
[5] S. Li, Fundamental research on the microstructure and properties evolution of nickel-based superalloy fabricated by selective laser melting, Huazhong University of Science and Technology, 2017.
[6] Z. Chen, S.G. Chen, Z.Y. Wei, et al., Anisotropy of nickel-based superalloy K418 fabricated by selective laser melting, Progr. Nat. Sci.: Mater. Int. 28 (4) (2018) 496–504.
[7] D.D. Gu, Q.M. Shi, K.J. Lin, et al., Microstructure and performance evolution and underlying thermal mechanisms of Ni-based parts fabricated by selective laser melting, Addit. Manuf. 22 (2018) 265–278.
[8] C.L. Qiu, H.X. Chen, Q. Liu, et al., On the solidification behaviour and cracking origin of a nickel-based superalloy during selective laser melting, Mater. Charact. 148 (2019) 330–344.
[9] L. Cao, F. Sun, T. Chen, et al., Quantitative prediction of oxide inclusion defects inside the casting and on the walls during cast-filling processes, Int. J. Heat Mass Transf. 119 (2018) 614–623.
[10] L. Cao, D.M. Liao, F. Sun, et al., Numerical simulation of cold-lap defects during casting filling process, Int. J. Adv. Manuf. Technol. 97 (2018) 2419–2430.
[11] P.P. Yuan, D.D. Gu, Molten pool behaviour and its physical mechanism during selective laser melting of TiC/AlSi10Mg nanocomposites: simulation and experiments, J. Phys. D Appl. Phys. 48 (3) (2015) 035303.
[12] Y.C. Wu, C.H. San, C.H. Chang, et al., Numerical modeling of melt-pool behavior in selective laser melting with random powder distribution and experimental validation, J. Mater. Process. Technol. 254 (2018) 72–78.
[13] D.Y. Zhang, P.D. Zhang, Z. Liu, et al., Thermofluid field of molten pool and its effects during selective laser melting (SLM) of Inconel 718 alloy, Addit. Manuf. 21 (2018) 567–578.
[14] T. Mukherjee, H.L. Wei, A. De, et al., Heat and fluid flow in additive manufacturing – Part I: Modeling of powder bed fusion, Comput. Mater. Sci. 150 (2018) 304–313.
[15] T. Mukherjee, H.L. Wei, A. De, et al., Heat and fluid flow in additive manufacturing – Part II: powder bed fusion of stainless steel, and titanium, nickel and aluminum base alloys, Comput. Mater. Sci. 150 (2018) 369–380.

[16] H.C. Tran, Y.L. Lo, Heat transfer simulations of selective laser melting process based on volumetric heat source with powder size consideration, J. Mater. Process. Technol. 255 (2018) 411–425.
[17] C. Bruna-Rosso, A.G. Demir, B. Previtali, Selective laser melting finite element modeling: Validation with high-speed imaging and lack of fusion defects prediction, Mater. Des. 156 (2018) 143–153.
[18] F.J. Gürtler, M. Karg, M. Dobler, et al., Influence of powder distribution on process stability in laser beam melting: analysis of melt pool dynamics by numerical simulations, in: Annual International Solid freeform fabrication symposium, 2014.
[19] K.H. Leitz, C. Grohs, P. Singer, et al., Fundamental analysis of the influence of powder characteristics in Selective Laser Melting of molybdenum based on a multi-physical simulation model, Int. J. Refract Metal Hard Mater. 72 (2018) 1–8.
[20] C. Panwisawas, C.L. Qiu, Y. Sovani, et al., On the role of thermal fluid dynamics into the evolution of porosity during selective laser melting, Scr. Mater. 105 (2015) 14–17.
[21] M. Markl, C. Körner, Multiscale modeling of powder bed-based additive manufacturing, Annu. Rev. Mater. Res. 46 (2016) 93–123.
[22] E.J.R. Parteli, T. Pöschel, Particle-based simulation of powder application in additive manufacturing, Powder Technol. 288 (2016) 96–102.
[23] Y.S. Lee, W. Zhang, Modeling of heat transfer, fluid flow and solidification microstructure of nickel-base superalloy fabricated by laser powder bed fusion, Addit. Manuf. 12 (2016) 178–188.
[24] S.A. Khairallah, A.T. Anderson, A. Rubenchik, et al., Laser powder-bed fusion additive manufacturing: Physics of complex melt flow and formation mechanisms of pores, spatter, and denudation zones, Acta Mater. 108 (2016) 36–45.
[25] C. Tang, J.L. Tan, C.H. Wong, A numerical investigation on the physical mechanisms of single track defects in selective laser melting, Int. J. Heat Mass Transf. 126 (2018) 957–968.
[26] C.W. Hirt, B.D. Nichols, Volume of fluid (VOF) method for the dynamics of free boundaries, J. Comput. Phys. 39 (1) (1981) 201–225.
[27] L. Cao, F. Sun, T. Chen, et al., Study on the numerical simulation of liquid-solid conversion affecting flow behavior during casting filling process, Acta Metall. Sin. 53 (11) (2017) 1521–1531.
[28] J.U. Brackbill, D.B. Kothe, C. Zemach, A continuum method for modeling surface tension, J. Comput. Phys. 100 (2) (1992) 335–354.
[29] J. Yang, F. Wang, 3D finite element temperature field modelling for direct laser fabrication, Int. J. Adv. Manuf. Technol. 43 (11–12) (2009) 1060–1068.
[30] L. Cao, D.M. Liao, Y.Z. Lu, et al., Heat transfer model of directional solidification by LMC process for superalloy casting based on finite element method, Metallur. Mater. Trans. A 47 (9) (2016) 4640–4647.